Nanoscale

PAPER

View Article Online
View Journal | View Issue

Cite this: *Nanoscale*, 2021, **13**, 20289

Janus silver/ternary silver halide nanostructures as plasmonic photocatalysts boost the conversion of CO_2 to acetaldehyde†

Henglei Jia, *‡ Yanrong Dou,‡ Yuanyuan Yang, Fan Li and Chun-yang Zhang *

Received 3rd September 2021,
Accepted 7th November 2021

DOI: 10.1039/d1nr05801k

rsc.li/nanoscale

Photocatalytic conversion of carbon dioxide (CO_2) to liquid product acetaldehyde (CH_3CHO) remains a great challenge due to the involvement of a complex 10-electron reduction process and a sluggish C–C coupling reaction. Herein, we report the synthesis of Janus silver/ternary silver halide (Ag/AgClBr) nanostructures through precisely manipulating the growth kinetics and its function as a plasmonic photocatalyst to boost the conversion of CO_2 to CH_3CHO. The obtained Janus nanostructures featuring both spatially separated architecture and broad light-harvesting capability facilitate the photocatalytic reduction of CO_2 under solar illumination. The photocatalytic CO_2 reduction with the characteristics of high activity and good selectivity can generate a 10-electron reduction product CH_3CHO with a generation rate of 209.3 ± 9.5 μmol h^{-1} g^{-1} and a selectivity of 96.9%, which are rarely achieved in previously reported photocatalytic CO_2 reduction systems. The excellent photocatalytic performance can be ascribed to the plasmonic effect of Ag nanocrystals and the favorable active sites on the catalyst surface. This research demonstrates for the first time the utilization of the Janus Ag/AgClBr nanostructures to generate the value-added C_2 liquid product through photocatalytic CO_2 reduction, paving the way for the design and construction of novel plasmonic photocatalysts.

Introduction

Solar-driven conversion of green-house gas carbon dioxide (CO_2) to chemical fuels and feedstocks is a potential strategy to address the energy and environmental challenges, opening a possibility of closing the anthropogenic carbon cycle in a renewable and sustainable way.[1–3] Despite substantial endeavors, it remains challenging to efficiently convert CO_2 to value-added fuels with high activity and good selectivity because of the thermodynamically stable and chemically inert property of the linear CO_2 molecules.[4] So far, semiconductor photocatalysts are widely applied in the photocatalytic CO_2 reduction due to their excellent stability and high reactivity, while the products are mainly limited to C_1 compounds such as CO, CH_4, and CH_3OH. The formation of C_2 products with high volumetric energy densities remains a great challenge due to the sluggish multielectron reduction dynamics process.[5–10] Acetaldehyde (CH_3CHO) is an important chemical industrially produced mainly by the Wacker process through the oxidation of ethylene.[11] The liquid product CH_3CHO is much more appealing in the CO_2 reduction because of its high energy density and ease of storage and transportation.[12,13] However, the efficient production of CH_3CHO through photocatalytic CO_2 reduction is rarely achieved because of the involvement of both 10-electron reduction and C–C coupling processes, which are much more complex and sluggish than those of C_1 products. Therefore, the synthesis of new efficient photocatalysts with the capability of reducing CO_2 to CH_3CHO with high activity and good selectivity is urgently needed.

The integration of plasmonic metals with semiconductors to obtain plasmonic photocatalysts has triggered increasing interest recently due to their potential for (1) promoting the photocatalytic activity through the localized surface plasmon resonance (LSPR) properties of plasmonic metals and (2) unlocking the reaction pathways by reducing the activation barriers.[14–20] Plasmonic metals (*e.g.*, Au, Ag, and Cu) are particularly attractive because of their strong resonant behaviors in response to ultraviolet, visible, and near-infrared light. Moreover, the integration of semiconductors with plasmonic metals can greatly enhance the photocatalytic performance

College of Chemistry, Chemical Engineering and Materials Science, Collaborative Innovation Center of Functionalized Probes for Chemical Imaging in Universities of Shandong, Key Laboratory of Molecular and Nano Probes, Ministry of Education, Shandong Provincial Key Laboratory of Clean Production of Fine Chemicals, Shandong Normal University, Jinan 250014, China. E-mail: hljia@sdnu.edu.cn, cyzhang@sdnu.edu.cn

†Electronic supplementary information (ESI) available. See DOI: 10.1039/d1nr05801k

‡These authors contributed equally to this work.

through different non-mutually exclusive energy-transfer mechanisms.[21–23] Among different plasmonic metals, Ag is a potential plasmonic photocatalyst for plasmon-driven CO_2 reduction because (1) Ag has the characteristics of favorable dielectric functions, nontoxicity, and relatively low cost;[24,25] (2) Ag possesses relatively large overpotential for the reduction of protons and can efficiently suppress the photocatalytic hydrogen production, which is a fiercely competing reaction with the photocatalytic CO_2 reduction;[26] (3) Ag can significantly improve the CH_3CHO selectivity in the CO_2 reduction by weakening the binding energy of the reduced CH_3CHO intermediates.[27,28] Moreover, silver halides (AgX) are promising semiconductor photocatalysts with a variety of photocatalytic applications.[29–33] In comparison with binary AgX, ternary AgX nanomaterials (*e.g.*, AgClBr) possess more energy states in the valence band and higher conduction band edges, making them excellent photocatalysts for CO_2 reduction.[34] We suppose that the integration of the AgX semiconductor nanocrystals with plasmonic Ag nanocrystals can obtain ternary AgX nanocrystals with enhanced photocatalytic performance and stability in the photocatalytic CO_2 reduction. However, the development of Ag/ternary AgX nanostructures toward photocatalytic CO_2 reduction (especially for the generation of C_2 products) has rarely been reported so far.

Herein, we report the synthesis of the Janus silver/ternary silver halide (Ag/AgClBr) nanostructure through precisely manipulating the growth kinetics and its function as a plasmonic photocatalyst to boost the conversion of CO_2 to CH_3CHO. The composition and light-harvesting property of the Janus nanostructures can be facilely adjusted by changing the molar ratios of feeding reagents in the precursors. The obtained Janus nanostructures featuring both spatially separated architecture and broad light-harvesting capability facilitate the photocatalytic reduction of CO_2 under solar illumination. The photocatalytic CO_2 reduction with the characteristics of high activity and good selectivity can generate a 10-electron reduction product CH_3CHO with a generation rate of 209.3 ± 9.5 μmol h^{-1} g^{-1} and a selectivity of 96.9%, which are rarely achieved in previously reported photocatalytic CO_2 reduction systems.

Henglei Jia

I received my Ph.D. degree in Materials Science and Engineering from The Chinese University of Hong Kong (CUHK) in 2016, followed by a postdoctoral study in CUHK. In 2017, I joined the College of Chemistry, Chemical Engineering and Materials Science of Shandong Normal University as an assistance professor and was promoted to associate professor in 2019. Currently, my research interest focuses on the design and controllable synthesis of colloidal noble metal nanocrystals, metal/semiconductor hybrid nanostructures, 2D ultrathin alloy nanomaterials, and their performances in various catalytic and energy conversion applications.

Results and discussion

The Janus nanostructures are obtained through the co-precipitation reaction by titrating $AgNO_3$ into an ethylene glycol solution composed of Br^- and Cl^- ions. The injection rate and reaction dynamics can be precisely controlled using a syringe pump. Ethylene glycol instead of water is used as the solvent in the whole process because of its relatively high viscosity which can significantly decrease the precipitation reaction rate, facilitating the nucleation/growth and the formation of ternary AgClBr nanocrystals.[34] The composition of the ternary AgClBr nanocrystals can be adjusted by simply changing the molar ratios of the halide ions in the precursors. In addition, ethylene glycol may serve as a weak reductant in the presence of polyvinylpyrrolidone (M_w = 40 000).[35] It can reduce $AgNO_3$ to tiny Ag nanoclusters that subsequently grow into Ag nanocrystals on the surface of the ternary AgClBr nanocrystals through a self-catalytic reduction process.[34] Consequently, the Janus nanostructures with Ag and ternary AgClBr nanodomains distributed onto the same surface are successfully synthesized. The obtained Janus nanostructures are named Ag/$AgCl_xBr_{(1-x)}$, where the subscripts are determined by the X-ray photoelectron spectroscopy (XPS) results (Fig. S1 and Table S1†), which will be discussed later.

Fig. 1a displays a representative low-magnification transmission electron microscopy (TEM) image of the as-obtained Janus Ag/$AgCl_{0.79}Br_{0.21}$ nanostructures with excellent monodispersion and high number yield of Janus nanostructures. Each asymmetric nanostructure comprises two segregated nanodomains and a shared interface in contact with each other. The sizes of the Ag nanocrystals and ternary AgClBr nanocrystals are 21.5 ± 3.1 nm and 24.8 ± 4.8 nm, respectively. A plasmon peak located at 359 nm appears in the extinction spectrum (Fig. 1b), indicating the presence of Ag nanocrystals in the Janus nanostructures.[21] Moreover, the Janus nanostructures possess a wide light-harvesting range that spans the ultraviolet, visible and near-infrared regions (Fig. 1b), suggesting that the ternary AgClBr nanocrystals can respond to the visible and near-infrared light, which is critical for the solar-driven photocatalysis. Both the LSPR property of plasmonic Ag nanocrystals and the wide light-harvesting range of ternary AgClBr nanocrystals endow the Janus nanostructures with the capability of efficiently harvesting solar energy. Furthermore, high-angle annular dark-field scanning transmission electron microscopy (HAADF-STEM) imaging, energy-dispersive X-ray (EDX) spectroscopy mapping, and high-resolution TEM (HRTEM) imaging were conducted to investigate the Janus feature (Fig. 1c and d). The EDX mapping indicates that element Ag disperses on both sides while elements Br and Cl are mainly

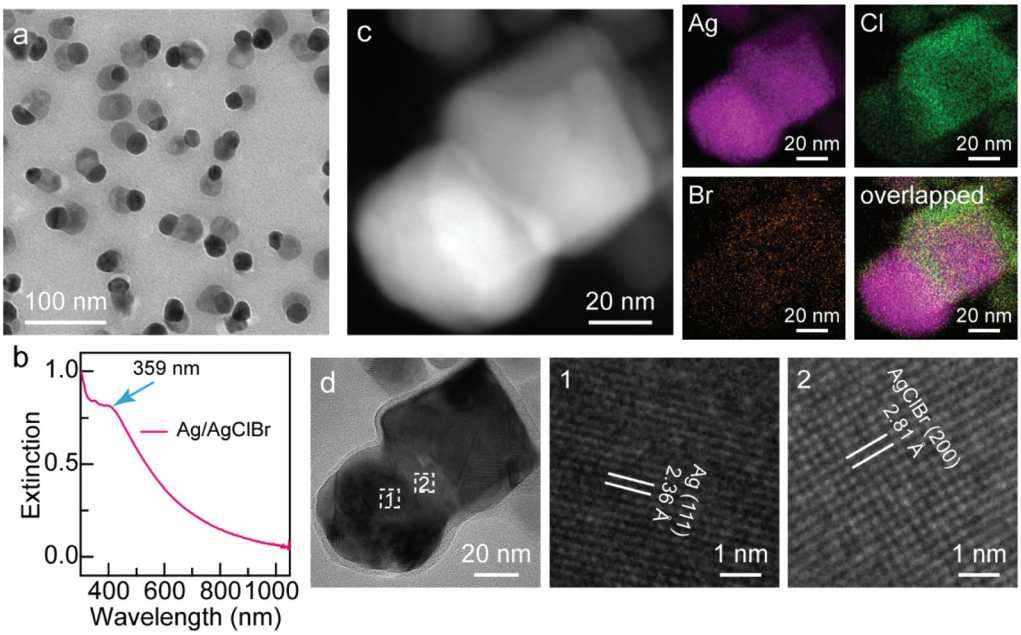

Fig. 1 Janus Ag/AgClBr nanostructures. TEM image (a) and extinction spectrum (b) of the as-obtained Ag/$AgCl_{0.79}Br_{0.21}$ nanostructures. (c) HAADF-STEM image (left) and the corresponding EDX maps of a representative Janus Ag/$AgCl_{0.79}Br_{0.21}$ heterostructure. (d) HRTEM image of a single Janus Ag/$AgCl_{0.79}Br_{0.21}$ nanostructure. Two typical regions marked by dashed white boxes (1 and 2) and the corresponding enlarged images verify the facets of Ag and AgClBr.

located on one side of the Janus nanostructure (Fig. 1c), confirming that the two sides of the Janus structure are Ag and ternary AgClBr, respectively. The lattice fringes taken from the HRTEM image reveal that the one side of the Janus nanostructure is made of metallic Ag and the other side is composed of ternary AgClBr (Fig. 1d), further verifying that the two sides of the Janus nanostructures are Ag nanocrystals and ternary AgClBr alloy nanocrystals, respectively.

X-ray diffraction (XRD) and XPS were carried out to investigate the crystalline nature and chemical composition of the Janus nanostructures. As shown in the XRD result (Fig. 2a), the diffraction peaks of the Janus Ag/$AgCl_{0.79}Br_{0.21}$ nanostructures can be indexed according to the cubic structure of Ag (space group, $Fm\bar{3}m$; lattice constant, 0.408 nm) and cubic structure of AgClBr (space group, $Fm\bar{3}m$; lattice constant, 0.5626 nm), respectively. The XPS survey spectrum demonstrates the existence of the elements Ag, Br, and Cl in the sample (Fig. 2b), with the signals of C and O coming from the surfactant molecules and the signal of Si originating from the Si substrate. The high-resolution Ag 3d XPS spectrum can be fitted with two types of Ag components (Ag^0 and Ag^+) (Fig. 2c). The peaks located at 367.4 eV and 373.4 eV are attributed to the binding energies of Ag $3d_{5/2}$ and Ag $3d_{3/2}$ of Ag^+ in the AgClBr nanocrystals, whereas the peaks at 367.8 eV and 373.8 eV are assigned to the pure metallic Ag nanocrystals.[36] The high-resolution Br 3d (68.3 eV and 69.2 eV) (Fig. 2d) and Cl 2p (197.7 eV and 199.3 eV) (Fig. 2e) XPS spectra suggest that the valence states of Br and Cl in Janus nanostructures are both −1 state.[37] In addition, the molar ratios of Cl to Br can be calculated by integrating the peak areas. All the sample names in this work are therefore determined on the basis of XPS results (Fig. S1 and Table S1†).

Since the morphological and structural properties of the Janus Ag/AgClBr nanostructures are highly sensitive to the reaction dynamics, we performed a series of control experiments to elucidate the effects of kinetic factors upon the growth behavior of Janus nanostructures. Firstly, we investigated the effect of the Cl/Br molar ratio upon the structural and optical properties by changing the molar ratio of Br^- and Cl^- ions and keeping the total halide ion amount constant in the reaction solution (Fig. S2–S4†). Although the Janus morphology can be obtained with different Cl/Br molar ratios, their optical and structural properties are significantly different. With the increase of the Cl/Br ratio, the plasmon peaks of Ag nanocrystals become more and more obvious (Fig. 1b and S3†), suggesting the formation of Ag nanocrystals in the Janus nanostructures. This conclusion is supported by the XRD results that the intensities of metallic Ag peaks enhance with the increase of Cl/Br molar ratios (Fig. 2a and S4†). Simultaneously, the crystalline phases of AgX change from AgBr to AgClBr and eventually to AgCl. Secondly, we studied the effect of the Ag/halide (Ag/X) ratio by changing the amount of $AgNO_3$ and keeping the total halide ion amount constant (Fig. S5–S7†). When the Ag/X ratio is smaller than 1 : 1, the Janus nanostructures can hardly be obtained, with neither an Ag plasmon peak in the extinction spectra (Fig. S6†) nor a metallic Ag peak in the XRD patterns (Fig. S7†) being observed. In contrast, the addition of sufficient $AgNO_3$ amount

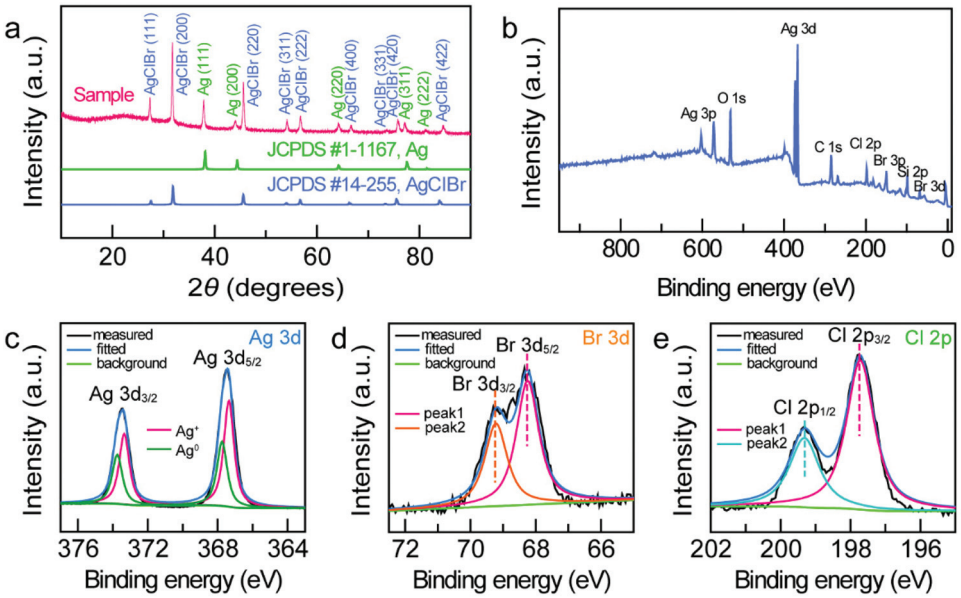

Fig. 2 Structure and composition of the Janus Ag/AgClBr nanostructures. (a) XRD patterns of the Janus Ag/$AgCl_{0.79}Br_{0.21}$ nanostructures. XPS survey spectrum (b) and high-resolution Ag 3d (c), Br 3d (d), and Cl 2p (e) XPS spectra of the Janus Ag/$AgCl_{0.79}Br_{0.21}$ nanostructures.

results in the red-shift of the plasmon peak of Ag nanocrystals in the extinction spectra and the increase of the metallic Ag peak in the XRD patterns due to the increased size of Ag nanocrystals induced by the increasing $AgNO_3$ amount. Thirdly, we investigated the effect of the injection rate of $AgNO_3$ (Fig. S8–S10†). The results suggest that an appropriate injection rate (0.4–0.8 ml min^{-1}) is critical to the formation of the Janus nanostructures. Above all, the morphological and structural properties are highly dependent on the Cl/Br molar ratio, Ag/X molar ratio and the injection rate of $AgNO_3$.

The spatial architecture plays a significant role in the photocatalytic performance of the plasmonic photocatalysts.[16,38–40] The spatially separated design and excellent light-harvesting capability of the Janus Ag/AgClBr nanostructures facilitate the plasmon-driven photocatalytic CO_2 reduction under solar illumination. The photocatalytic experiments were conducted in CO_2-saturated $KHCO_3$ aqueous solution (0.1 M, 20 mL) under AM 1.5G 1 sun illumination at an optical power density of 100 mW cm^{-2}, with triethylamine as the hole sacrificial agent. The products were analyzed by off-line gas chromatography in combination with ion chromatography.

AgX has been attracting increasing interest in the photocatalytic CO_2 reduction owing to their excellent electronic structures. Halides may also act as the active sites by modulating the adsorbed CO_2 and intermediate molecular configuration, which can efficiently reduce the activation barrier and improve the photocatalytic performance.[41–43] In comparison with binary AgX, the ternary AgX is a more promising photocatalyst owing to its unique merit of facile modulation of electronic structures.[34] In this regard, we first evaluated the photocatalytic performance of five types of Janus Ag/AgX nanostructures with different Cl/Br molar ratios, including Ag/AgBr, Ag/$AgCl_{0.17}Br_{0.83}$, Ag/$AgCl_{0.45}Br_{0.55}$, Ag/$AgCl_{0.79}Br_{0.21}$, and Ag/AgCl. To our surprise, CH_3CHO produced through the 10-electron reduction process, which has rarely been reported in previous photocatalytic systems, is the dominant product for all these five catalysts (Fig. 3a). The Janus Ag/$AgCl_{0.79}Br_{0.21}$ nanostructures exhibit optimal photocatalytic activity toward CH_3CHO production with a generation rate of 209.3 ± 9.5 μmol h^{-1} g^{-1}, which is 6.2-fold compared with that of the Janus Ag/AgBr nanostructures. The CH_3CHO production rate on the Janus Ag/$AgCl_{0.79}Br_{0.21}$ nanostructures is comparable or even superior to those representative works reported recently (Table S2†). Besides the liquid product CH_3CHO, other three gas products including CO, CH_4, and C_2H_4 are all detected in these systems. But H_2 is not detected in our system, suggesting that the photocatalytic hydrogen evolution is suppressed by the reduction of CO_2.[44] The selectivity of CH_3CHO was evaluated on the basis of the consumed electrons (see the experimental section for details).[45,46] The CH_3CHO selectivity is higher than 90% when the Cl/Br molar ratio is larger than 1 : 1, and reaches a maximum value of 96.9% at a Cl/Br molar ratio of about 8 : 2. Both the high activity and selectivity toward CH_3CHO production suggest that the two types of halide active sites synergistically promote the CO_2 activation and facilitate their conversion to the products. Since the Janus Ag/$AgCl_{0.79}Br_{0.21}$ nanostructures exhibit optimal photocatalytic activity and selectivity, we kept the Cl/Br molar ratio of the Janus nanostructures at 0.79 : 0.21 and investigated the effect of the Ag/X molar ratio upon the photocatalytic performance (Fig. 3b). When the Ag/X ratio in the precursor is 1 : 1, the catalyst exhibits optimal photocatalytic activity and selectivity toward CH_3CHO production. Therefore, the Janus Ag/$AgCl_{0.79}Br_{0.21}$ nanostructures are selected as the photocatalyst.

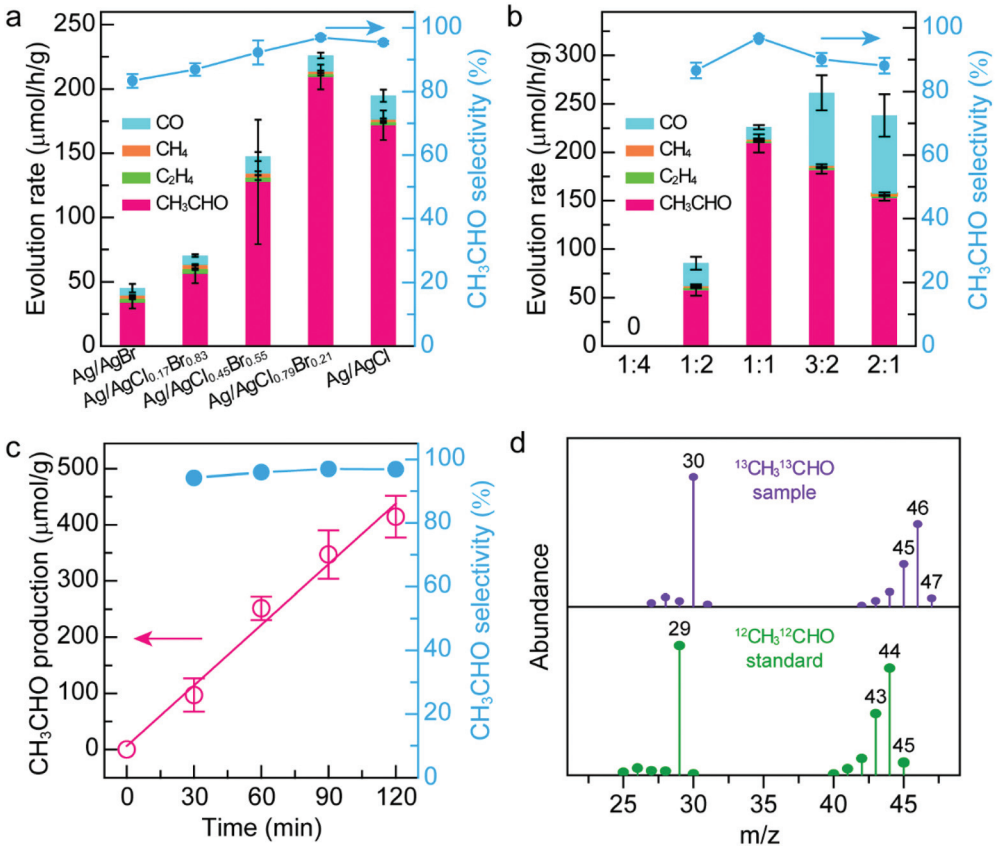

Fig. 3 Photocatalytic CO_2 reduction performances. Photocatalytic CO_2 reduction activity and CH_3CHO selectivity of the Janus Ag/AgClBr nanostructures with different Cl/Br molar ratios (a) and different Ag/X molar ratios (b). (c) Photocatalytic CH_3CHO production activity and selectivity of the Janus $Ag/AgCl_{0.79}Br_{0.21}$ nanostructures as a function of time. (d) Mass spectra extracted from the GC–MS analysis of $^{13}CH_3{}^{13}CHO$ (purple) and the standard mass spectra of $^{12}CH_3{}^{12}CHO$ (green).

Under solar illumination, the CH_3CHO production increases with the irradiation time, but the selectivity remains nearly constant (Fig. 3c). To reveal the origin of the produced CH_3CHO, various control experiments were performed (Fig. S11†). No CH_3CHO is detected under the following experimental conditions: (a) without a photocatalyst, (b) in the dark, and (c) under an Ar atmosphere, suggesting that the boosting of the CH_3CHO product originates from the photocatalytic reduction of CO_2 induced by the catalyst. The photocatalyst activity decreases by 15.3% in the absence of a hole sacrificial agent, indicating that the use of a sacrificial agent can efficiently reduce the hot carrier recombination and facilitate the CO_2 reduction by electrons. To further trace the carbon source of product CH_3CHO, we carried out a $^{13}CO_2$ isotope labelling experiment (Fig. 3d and Fig. S12†). As displayed in Fig. S12a,† only product CH_3CHO is detected besides the hole scavenger ($(C_2H_5)_3N$) in gas chromatography spectra of the reaction solution, suggesting that CH_3CHO is the only liquid product of the photocatalytic CO_2 reduction. The mass spectra of CH_3CHO and $(C_2H_5)_3N$ were extracted from the gas chromatography–mass spectrometry (GC–MS) analysis (Fig. 3d and Fig. S12b†). All the ion fragment peaks of the generated CH_3CHO under a $^{13}CO_2$ atmosphere exhibit clear shifts in comparison with those of the standard fragmentation pattern of $^{12}CH_3{}^{12}CHO$ (Fig. 3d), demonstrating that the generated CH_3CHO is definitely derived from the photocatalytic CO_2 reduction. Note that the presence of a hole scavenger has no apparent influence on the mass spectra of the liquid product (Fig. S12b†). To clarify the role of Ag nanocrystals played in the photocatalytic CO_2 reduction, the $AgCl_{0.8}Br_{0.2}$ sample was prepared through a co-precipitation approach[47] and its photocatalytic performance was studied (Fig. S13†). As shown in Fig. S13c,† the photocatalytic activity and selectivity of the AgClBr sample toward the reduction of CO_2 are 52.9 ± 4.2 μmol h^{-1} g^{-1} and 78.3%, greatly lower than those of the Janus Ag/AgClBr nanostructures. The poor photocatalytic performance of the AgClBr sample reveals the importance of the plasmonic effect of Ag nanocrystals in the photocatalytic process. In addition, the Janus nanostructures exhibit excellent recyclability and photostability during photocatalytic CO_2 reduction. After three successive cycles, the photocatalytic activity remains at 87.5%, and the selectivity of CH_3CHO remains almost constant (Fig. S14†). Moreover, no morphological and structural change is observed after the typical reaction process, suggesting the excellent photostability of Janus nanostructures (Fig. S15 and S16†).

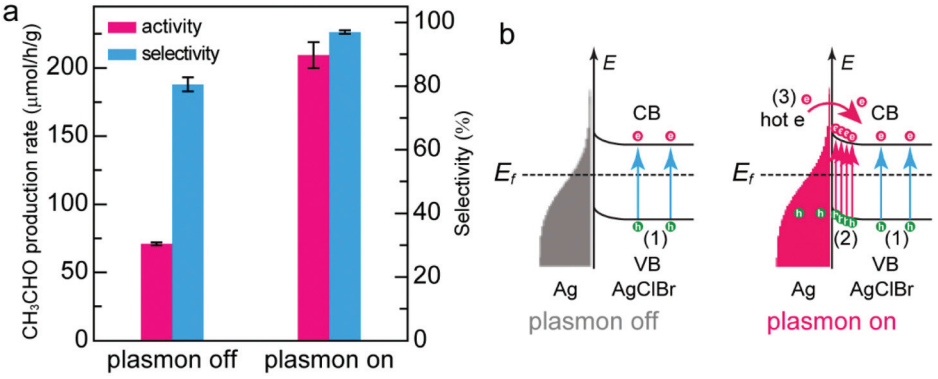

Fig. 4 Plasmonic effect on the photocatalytic performance. (a) Comparison of the photocatalytic CH_3CHO production activity and selectivity of the Janus $Ag/AgCl_{0.79}Br_{0.21}$ nanostructures under different light irradiation. (b) Plasmonic effect on the hot carrier generation. E_f, Fermi level; CB, conduction band; VB, valence band.

To investigate the plasmonic effect of the Janus nanostructure photocatalyst, we evaluated the photocatalytic performance under solar or $\lambda > 420$ nm light irradiation. Since the plasmon peak of Ag nanocrystals is located at 359 nm (Fig. 1a), LSPR of Ag nanocrystals almost takes no effect under $\lambda >$ 420 nm light irradiation (plasmon off state). In contrast, LSPR of Ag nanocrystals is active under solar irradiation (plasmon on state). As shown in Fig. 4a, the photocatalytic activity and selectivity of the Janus nanostructures toward CH_3CHO production under the plasmon-off state are 71.1 ± 1.2 μmol h^{-1} g^{-1} and 80.6%, much lower than those under the plasmon-on state. The photocatalytic activity under the plasmon-off state decreases by 66% compared with that under the plasmon-on state, suggesting that the plasmonic effect plays a critical role in the photocatalytic CO_2 reduction process. The significant difference in the photocatalytic performance under these two states can be explained by their different reaction mechanisms (Fig. 4b). Under the plasmon-off state, the ternary AgClBr semiconductor in the Janus nanostructures is excited to generate the electron/hole pairs in the semiconductor component (mechanism 1 in Fig. 4b). The generated electrons participate in the reduction of CO_2 and the holes are consumed by the hole scavengers. Ag nanocrystals function as the cocatalyst in this scenario. In contrast to the plasmon-off state, there are three possible reaction mechanisms under the plasmon-on state. Under solar irradiation, both plasmonic Ag nanocrystals and ternary AgClBr semiconductors can be excited. Similar to the plasmon-off state, the electron/hole pairs are generated in the semiconductor component (mechanism 1 in Fig. 4b). Simultaneously, a strong local electromagnetic field that is orders of magnitude larger than the photon field is generated in the near-field region of Ag nanocrystals due to their LSPR properties.[21,22] The part of the semiconductor close to the metal/semiconductor interface is subjected to the strong electric fields. Since the electron–hole formation rate is proportional to the local electric field intensity, the hot carrier concentration in this region is greatly boosted (mechanism 2 in Fig. 4b). Moreover, electron/hole pairs can be generated in plasmonic Ag nanocrystals under resonance excitation. Hot electrons with sufficient energy can be injected into the conduction band of the semiconductor and take part in the CO_2 reduction process (mechanism 3 in Fig. 4b). Besides, the photothermal contribution from the Ag nanocrystals is believed to be very low owing to the use of a circulation cooling system. Among these three hot carrier generation processes, the improvement of photocatalytic activity under the plasmon-on state should mainly benefit from the near-field electromagnetic mechanism (mechanism 2 in Fig. 4b), which promotes the formation of the electron/hole pairs and boosts the generation of the CH_3CHO product. In addition, the selectivity increases under the plasmon-on state, because the plasmonic effect can unlock the reaction pathways to facilitate the product conversion.[15] On the basis of the above results, we can conclude that the conversion of CO_2 to CH_3CHO takes place at the AgBrCl surface, since CH_3CHO can be produced under the situation of plasmon on or plasmon off. Although it has still remained elusive to tell the true active sites for the CO_2 reduction, it is believed that the major active sites for the CH_3CHO formation are located at the Ag/AgBrCl interface because of the two following reasons. First, theoretical calculations have proved that the energy bandgaps and electronic structures can be facilely adjusted through the substitution of Cl atoms by Br atoms in the AgX semiconductor, facilitating the CO_2 adsorption and conversion.[34,48] Second, the presence of metallic Ag on the AgBrCl surface can fill midgaps with additional energy states,[34] which can not only improve the light-harvesting of the AgBrCl catalyst but also promote the photocatalytic activity. According to the near-field electromagnetic mechanism, the hot carrier concentration close to the Ag/AgBrCl interface is greatly boosted. Benefiting from more available energy states and the presence of metallic Ag in this region, the reduction of CO_2 mainly takes place at the interface of Ag/AgBrCl.

The adsorption and activation of CO_2 molecules play irreplaceable roles in the photocatalytic CO_2 reduction due to the thermodynamically stable and chemically inert properties of

the CO_2 molecules. The bending of the linear CO_2 molecules and even the cleavage of C=O bonds must overcome a large activation barrier,[49] which can be largely reduced by the introduction of active sites on the catalyst surface.[50–52] To investigate the excellent photocatalytic performance on the Janus nanostructures, *in situ* Fourier transform infrared (FT-IR) spectroscopy was employed to precisely track the reaction intermediates during the photocatalytic CO_2 reduction process. As shown in Fig. 5, *in situ* FT-IR spectra of the reaction solution are collected as a function of irradiation time. The bands of 1000–2200 cm^{-1} region originate from the carbonate adsorbates of CO_2, and the peaks at 1551, 1312, and 1730 cm^{-1} correspond to monodentate carbonate (m-CO_3^{2-}), bidentate carbonate (b-CO_3^{2-}), and chelating-bridged carbonate (c-CO_3^{2-}) adsorbed on the catalyst surface, respectively.[42,53]

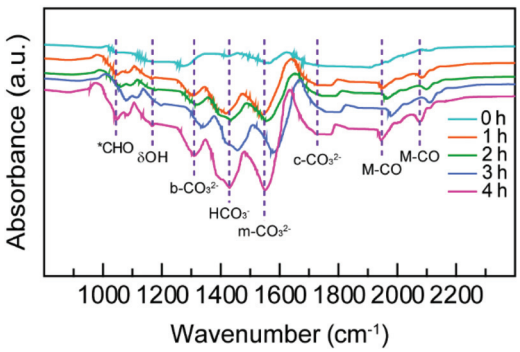

Fig. 5 *In situ* FT-IR spectra recorded as a function of time during the photocatalytic CO_2 reduction on the Janus Ag/$AgCl_{0.79}Br_{0.21}$ nanostructures.

The presence of various carbonate species suggests that CO_2 can be adsorbed and activated on the catalyst surface in different modes. The irradiation time-dependent increase in peak intensity indicates the boosting of activated CO_2 molecules on the catalyst. In addition, the peaks at 1430 and 1167 cm^{-1} are assigned to the $\nu_{as}(CO_3)$ and δ(OH) modes of bicarbonates (HCO_3^-), which originate from the interaction of the adsorbed CO_2 and H_2O on the catalyst surface.[42,54] The appearance of the 1048 cm^{-1} peak indicates the generation of *CHO.[54] The two peaks at 1946 and 2076 cm^{-1} result from the Ag-CO adsorbed species, suggesting the existence of *CO intermediates in the photocatalytic process. The above FT-IR results demonstrate that the catalyst surface facilitates both the adsorption/activation of CO_2 molecules and the generation of the product.

Based on the above results, we proposed a hypothetical photocatalytic CO_2 reduction mechanism for Janus Ag/AgClBr nanostructures. The surface of AgClBr nanocrystals possesses a large number of accessible active sites. Once CO_2 molecules interact with these active sites, they are polarized to generate electron repulsion that can bend the linear molecular structure. In comparison with the linear structure, the bent CO_2 molecules greatly decrease their lowest unoccupied molecular orbital level to favour the electron injection from the plasmonic photocatalyst. Subsequently, hot carriers are generated according to different mechanisms under solar irradiation (Fig. 4b). The photogenerated electrons transfer to the lowest unoccupied molecular orbital, enabling the conversion of CO_2 molecules to different intermediates. Fig. 6 displays the reaction pathways for the reduction of CO_2 to CH_3CHO product. The whole process can be divided into three stages including (1) the generation of C_1 intermediates (Fig. 6a and b), (2) C–C coupling of two adjacent C_1 intermediates (Fig. 6c), and the

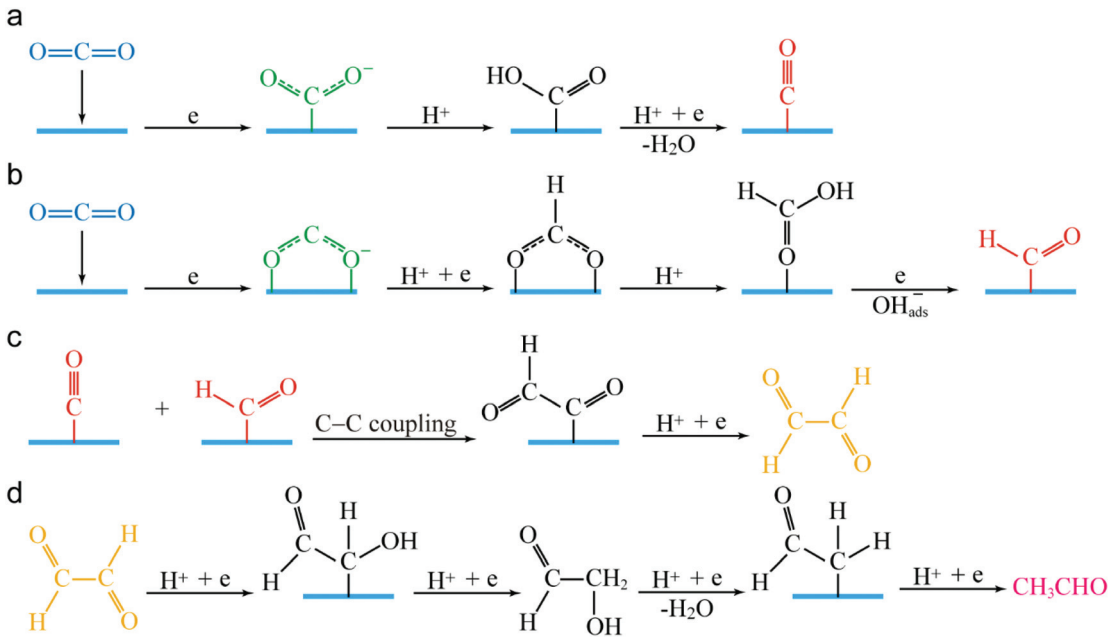

Fig. 6 Reaction pathways for the photocatalytic reduction of CO_2 to CH_3CHO product.

conversion of C_2 intermediates to the CH_3CHO product (Fig. 6d). It is generally accepted that the formation of one-electron reduction product $CO_2^{\bullet-}$ is thermodynamically unfavourable but is the prerequisite for the CO_2 conversion.[49] This process is achieved through the adsorption of CO_2 on the active sites and reduction by photogenerated electrons under solar irradiation. Owing to the various binding modes of CO_2 molecules on the Janus Ag/AgClBr nanostructures, monodentate and bidentate binding of $CO_2^{\bullet-}$ are mainly formed on the active sites (green color in Fig. 6a and b) and the $CO_2^{\bullet-}$ intermediates are subsequently converted to two different C_1 intermediates including *CO and *CHO (red color in Fig. 6a and b), as revealed by the *in situ* detection results. In addition, a C_2 intermediate glyoxal (CHOCHO, yellow color in Fig. 6c) can be formed through dimerization of two *CHO or C–C coupling between *CO and *CHO.[2,55,56] To gain a deep insight into the reaction pathways, the theoretical calculation was conducted to reveal the C–C coupling mode of CH_3CHO formation (Fig. S17†). Evidently, the C–C coupling mode between *CO and *CHO is thermodynamically more favorable than the dimerization of two *CHO. The glyoxal is therefore formed through the C–C coupling process (Fig. 6c). Eventually, the liquid product CH_3CHO is produced through subsequent stepwise hydrogenation (Fig. 6d).

Conclusions

In summary, we developed a facile method to synthesize the Janus Ag/AgClBr nanostructures and systematically investigated the photocatalytic performance of the Janus nanostructures as the plasmonic photocatalysts to boost the conversion of CO_2 to CH_3CHO. By precisely controlling the reaction conditions, we successfully synthesized the Janus nanostructures composed of Ag nanocrystals and ternary AgClBr alloy nanocrystals with a sharing interface. The obtained Janus nanostructures possess spatially separated morphology and wide light-harvesting capability, endowing them with a unique photocatalytic property to reduce CO_2 under solar illumination. The photocatalytic CO_2 reduction with the characteristics of high activity and good selectivity can generate a 10-electron reduction product CH_3CHO with a generation rate of 209.3 ± 9.5 μmol h^{-1} g^{-1} and a selectivity of 96.9%. The excellent photocatalytic performance can be ascribed to the plasmonic effect of Ag nanocrystals and the favorable active sites on the catalyst surface. A rational reaction mechanism for the photocatalytic CO_2 reduction to the CH_3CHO product has been proposed. This research provides a new strategy to synthesize efficient plasmonic photocatalysts for photocatalytic reduction of CO_2 to CH_3CHO, paving the way for fully utilizing solar energy to drive valuable chemical conversions.

Experimental

Chemicals

Polyvinylpyrrolidone (PVP, M_w = 40 000), potassium bicarbonate ($KHCO_3$, 99.7%), and silver nitrate ($AgNO_3$, ≥99.0%) were purchased from Sigma-Aldrich. Potassium bromide (KBr), sodium chloride (NaCl), ethylene glycol ($C_2H_6O_2$), and triethylamine (TEA) were obtained from Sinopharm Chemical Reagent. Carbon dioxide (CO_2, 99.999%), nitrogen (N_2, 99.999%), hydrogen (H_2, 99.999%), argon (Ar, 99.999%), and helium (He, 99.999%) were used as received. $^{13}CO_2$ (^{13}C, 99.0%; ^{18}O, <3%) was purchased from Aldrich. Deionized water with a resistivity of 18.2 MΩ cm was used in all experiments.

Synthesis of the Janus Ag/AgClBr nanostructures

Taking the synthesis of Janus $Ag/AgCl_{0.79}Br_{0.21}$ nanostructures as an example, NaCl (0.26 mmol), KBr (0.065 mmol) and PVP (2.5 g, M_w = 40 000) were added into $C_2H_6O_2$ (12 mL) in a 25 mL three-necked round-bottom flask. The mixture was heated and refluxed in an oil bath at 60 °C under magnetic stirring. After the complete dissolution of solid powders, $AgNO_3$ solution (0.34 M in $C_2H_6O_2$, 1 mL) was titrated into the solution mixture using a syringe pump (LSP02-1B, LongerPump) at a rate of 0.6 mL min^{-1}. The resultant solution was kept stirring for 2 h in a 60 °C oil bath. The whole process was conducted in the dark and protected with N_2. The synthesis of other Janus nanostructures was similar to that of the Janus $Ag/AgCl_{0.79}Br_{0.21}$ nanostructures except the change of the Cl/Br or Ag/X molar ratio.

Photocatalytic CO_2 reduction experiment

The photocatalytic CO_2 reduction reactions were performed in a customized gastight reaction system (65 mL) equipped with a quartz window on the top and an inlet and an outlet on the side. For a typical photocatalytic reaction, the photocatalyst (40 mg) was dispersed into a solution mixture (20 mL) containing $NaHCO_3$ (0.1 M) and TEA (1 mL). TEA was employed as the hole scavenger. Prior to the irradiation, the solution was bubbled with high-purity CO_2 gas (99.999%) for at least 30 min at a speed of 20 mL min^{-1} and the final pressure in the reaction system was maintained at 1 atm after closing the inlet and outlet. A 500 W Xenon lamp (CEL-S500, CEAULIGHT) equipped with an AM 1.5G filter (100 mW cm^{-2}) was used as the light source for illumination and a circulation cooling system was employed to control the reaction temperature at 25 °C. The photocatalytic products were quantitatively analyzed using an off-line gas chromatograph (Agilent Technologies 7890B) equipped with a thermal conductivity detector (TCD) and a flame ionization detector (FID). He gas (99.999%) or H_2 gas (99.999%) was utilized as the carrier gas. The selectivities of the products were calculated on the basis of the consumed electrons.[45,46] Taking CH_3CHO as an example, its selectivity can be calculated as follows.

$$\text{Selectivity}_{CH_3CHO} = \frac{[10n(CH_3CHO)]}{[2n(CO)+8n(CH_4)+10n(CH_3CHO)+12n(C_2H_4)]} \times 100\%$$

where n(CO), n(CH_4), n(CH_3CHO), and n(C_2H_4) are the amounts (moles) of the products CO, CH_4, CH_3CHO, and C_2H_4

formed in the photocatalytic CO_2 reduction reaction. The $^{13}CO_2$ isotope labeling experiment was carried out under the same conditions except that $^{12}CO_2$ was replaced by $^{13}CO_2$, and the liquid products were detected by gas chromatography–mass spectrometry (GC–MS, Agilent 7697-5975C).

Calculation details

The density functional theory (DFT) calculations were conducted with the Vienna *Ab Initio* Simulation Package.[57,58] The ionic cores and valence electrons were described using the projected augmented wave potentials.[59,60] The exchange correlation interaction was solved by the Perdew–Burke–Ernzerhof formulation.[61] The plane wave cutoff energy was set at 400 eV. The classical rock-salt type AgCl unit cell was employed to demonstrate the equilibrium lattice constant. The constant was further optimized with a 9 × 9 × 9 Monkhorst–Pack *k*-point grid for Brillouin zone sampling to be a = 5.527 Å. The catalyst surface was modelled with a 2 × 2 periodicity in the x and y directions and 2 stoichiometric layers (4 atomic layers) in the z direction. This surface model consists of 32 Ag and 32 Cl atoms and 6 Cl atoms were replaced by Br atoms. The free energy of each reaction intermediate on the catalyst surface was calculated according to the equation $G = E + \mathrm{ZPE} - \mathrm{TS}$, where E is the electronic energy, ZPE is the zero-point energy, and TS is the entropy contribution.

Characterization

TEM imaging was performed on an HT7700 electron microscope at 100 kV. HRTEM, HAADF-STEM imaging and EDX mapping were carried out on an FEI Talos F200S microscope. Scanning electron microscopy (SEM) imaging was conducted on a Hitachi SU8010 microscope. The extinction spectra were recorded using a Hitachi U-3900 ultraviolet/visible/NIR spectrophotometer. XRD patterns were conducted on a Smart Lab Se diffractometer equipped with Cu Kα radiation. XPS spectra were recorded on a Thermo Scientific ESCALAB 250Xi spectrometer. *In situ* FT-IR spectra were obtained on a Nicolet 6700 spectrometer.

Conflicts of interest

There are no conflicts to declare.

Acknowledgements

This work was supported by the National Natural Science Foundation of China (Grant No. 21735003), the Natural Science Foundation of Shandong Province (No. ZR2020MB040), and the Award for Team Leader Program of Taishan Scholars of Shandong Province, China.

Notes and references

1 S. Z. Xu and E. A. Carter, *Chem. Rev.*, 2019, **119**, 6631–6669.
2 T. T. Kong, Y. W. Jiang and Y. J. Xiong, *Chem. Soc. Rev.*, 2020, **49**, 6579–6591.
3 Z. Jiang, X. H. Xu, Y. H. Ma, H. S. Cho, D. Ding, C. Wang, J. Wu, P. Oleynikov, M. Jia, J. Cheng, Y. Zhou, O. Terasaki, T. Y. Peng, L. Zan and H. X. Deng, *Nature*, 2020, **586**, 549–554.
4 W. G. Tu, Y. Zhou and Z. G. Zou, *Adv. Mater.*, 2014, **26**, 4607–4626.
5 W. Wang, C. Y. Deng, S. J. Xie, Y. F. Li, W. Y. Zhang, H. Sheng, C. C. Chen and J. C. Zhao, *J. Am. Chem. Soc.*, 2021, **143**, 2984–2993.
6 S. M. Sun, M. Watanabe, J. Wu, Q. An and T. Ishihara, *J. Am. Chem. Soc.*, 2018, **140**, 6474–6482.
7 M.-P. Jiang, K.-K. Huang, J.-H. Liu, D. Wang, Y. Wang, X. Wang, Z.-D. Li, X.-Y. Wang, Z.-B. Geng, X.-Y. Hou and S.-H. Feng, *Chem*, 2020, **6**, 2335–2346.
8 E. Vahidzadeh, S. Zeng, A. P. Manuel, S. Riddell, P. Kumar, K. M. Alam and K. Shankar, *ACS Appl. Mater. Interfaces*, 2021, **13**, 7248–7258.
9 J. Albero, Y. Peng and H. García, *ACS Catal.*, 2020, **10**, 5734–5749.
10 S. J. Xie, W. C. Ma, X. J. Wu, H. K. Zhang, Q. H. Zhang, Y. D. Wang and Y. Wang, *Energy Environ. Sci.*, 2021, **14**, 37–89.
11 J. A. Keith and P. M. Henry, *Angew. Chem., Int. Ed.*, 2009, **48**, 9038–9049.
12 I. Shown, S. Samireddi, Y.-C. Chang, R. Putikam, P.-H. Chang, A. Sabbah, F.-Y. Fu, W.-F. Chen, C.-I. Wu, T.-Y. Yu, P.-W. Chung, M. C. Lin, L.-C. Chen and K.-H. Chen, *Nat. Commun.*, 2018, **9**, 169.
13 X. Z. Qian, W. Y. Yang, S. Gao, J. Xiao, S. Basu, A. Yoshimura, Y. F. Shi, V. Meunier and Q. Li, *ACS Appl. Mater. Interfaces*, 2020, **12**, 55982–55993.
14 K. Awazu, M. Fujimaki, C. Rockstuhl, J. Tominaga, H. Murakami, Y. Ohki, N. Yoshida and T. Watanabe, *J. Am. Chem. Soc.*, 2008, **130**, 1676–1680.
15 E. Cortés, *Science*, 2018, **362**, 28–29.
16 H. L. Jia, A. X. Du, H. Zhang, J. H. Yang, R. B. Jiang, J. F. Wang and C.-Y. Zhang, *J. Am. Chem. Soc.*, 2019, **141**, 5083–5086.
17 S. J. Tan, A. Argondizzo, J. D. Ren, L. M. Liu, J. Zhao and H. Petek, *Nat. Photonics*, 2017, **11**, 806–812.
18 S. S. Li, H. Huang, L. Shao and J. F. Wang, *ACS Nano*, 2021, **15**, 10759–10768.
19 Y. J. Ma, X. Z. Zhu, S. S. Xu, G. L. He, L. Yao, N. T. Hu, Y. J. Su, J. Feng, Y. F. Zhang and Z. Yang, *Appl. Catal., B*, 2018, **234**, 26–36.
20 Y. Z. Guo, J. H. Yang, D. H. Wu, H. Y. Bai, Z. Yang, J. F. Wang and B. C. Yang, *J. Mater. Chem. A*, 2020, **8**, 16218–16231.
21 S. Linic, P. Christopher and D. B. Ingram, *Nat. Mater.*, 2011, **10**, 911–921.
22 R. B. Jiang, B. X. Li, C. H. Fang and J. F. Wang, *Adv. Mater.*, 2014, **26**, 5274–5309.
23 W. B. Hou and S. B. Cronin, *Adv. Funct. Mater.*, 2013, **23**, 1612–1619.

24 Y. R. Wu, X. J. Sun, Y. Yang, J. M. Li, Y. Zhang and D. Qin, *Acc. Chem. Res.*, 2017, **50**, 1774–1784.
25 C. Liang, Z.-A. Lu, J. Wu, M.-X. Chen, Y. Y. Zhang, B. Zhang, G.-L. Gao, S. W. Li and P. Xu, *ACS Appl. Mater. Interfaces*, 2020, **12**, 54266–54284.
26 B. C. Yu, Y. Zhou, P. Li, W. G. Tu, P. Li, L. Q. Tang, J. H. Ye and Z. G. Zou, *Nanoscale*, 2016, **8**, 11870–11874.
27 L. Wang, D. C. Higgins, Y. F. Ji, C. G. Morales-Guio, K. Chan, C. Hahn and T. F. Jaramillo, *Proc. Natl. Acad. Sci. U. S. A.*, 2020, **117**, 12572–12575.
28 A. Herzog, A. Bergmann, H. S. Jeon, J. Timoshenko, S. Kühl, C. Rettenmaier, M. L. Luna, F. T. Haase and B. R. Cuenya, *Angew. Chem., Int. Ed.*, 2021, **60**, 7426–7435.
29 P. Wang, B. B. Huang, X. Y. Qin, X. Y. Zhang, Y. Dai, J. Y. Wei and M.-H. Whangbo, *Angew. Chem., Int. Ed.*, 2008, **47**, 7931–7933.
30 J. Jiang, H. Li and L. Z. Zhang, *Chem. – Eur. J.*, 2012, **18**, 6360–6369.
31 C. H. An, J. Z. Wang, W. Jiang, M. Y. Zhang, X. J. Ming, S. T. Wang and Q. H. Zhang, *Nanoscale*, 2012, **4**, 5646–5650.
32 H. Y. Li, T. S. Wu, B. Cai, W. G. Ma, Y. J. Sun, S. Y. Gan, D. X. Han and L. Niu, *Appl. Catal., B*, 2015, **164**, 344–351.
33 C. Y. Mao, Y. M. Xiang, X. M. Liu, Z. D. Cui, X. J. Yang, K. W. K. Yeung, H. B. Pan, X. B. Wang, P. K. Chu and S. L. Wu, *ACS Nano*, 2017, **11**, 9010–9021.
34 S. C. Abeyweera, K. D. Rasamani and Y. G. Sun, *Acc. Chem. Res.*, 2017, **50**, 1754–1761.
35 Y. G. Sun and Y. N. Xia, *Science*, 2002, **298**, 2176–2179.
36 M. L. Pang, J. Y. Hu and H. C. Zeng, *J. Am. Chem. Soc.*, 2010, **132**, 10771–10785.
37 W.-J. Ong, L. K. Putri, L.-L. Tan, S.-P. Chai and S.-T. Yong, *Appl. Catal., B*, 2016, **180**, 530–543.
38 M. Ha, J.-H. Kim, M. You, Q. Li, C. H. Fan and J.-M. Nam, *Chem. Rev.*, 2019, **119**, 12208–12278.
39 W. J. Xu, J. Jia, T. Wang, C. Li, B. W. He, J. P. Zong, Y. W. Wang, H. J. Fan, H. X. Xu, Y. H. Feng and H. Y. Chen, *Angew. Chem., Int. Ed.*, 2020, **59**, 22246–22251.
40 J. W. Hong, D. H. Wi, S.-U. Lee and S. W. Han, *J. Am. Chem. Soc.*, 2016, **138**, 15766–15773.
41 L. Hao, L. Kang, H. W. Huang, L. Q. Ye, K. L. Han, S. Q. Yang, H. J. Yu, M. Batmunkh, Y. H. Zhang and T. Y. Ma, *Adv. Mater.*, 2019, **31**, 1900546.
42 J. P. Sheng, Y. He, J. Y. Li, C. W. Yuan, H. W. Huang, S. Y. Wang, Y. J. Sun, Z. M. Wang and F. Dong, *ACS Nano*, 2020, **14**, 13103–13114.
43 Y.-Y. Li, J.-S. Fan, R.-Q. Tan, H.-C. Yao, Y. Peng, Q.-C. Liu and Z.-J. Li, *ACS Appl. Mater. Interfaces*, 2020, **12**, 54507–54516.
44 X. D. Li, Y. F. Sun, J. Q. Xu, Y. J. Shao, J. Wu, X. L. Xu, Y. Pan, H. X. Ju, J. F. Zhu and Y. Xie, *Nat. Energy*, 2019, **4**, 690–699.
45 A. Li, Q. Cao, G. Y. Zhou, B. V. K. J. Schmidt, W. J. Zhu, X. T. Yuan, H. L. Huo, J. L. Gong and M. Antonietti, *Angew. Chem., Int. Ed.*, 2019, **58**, 14549–14555.
46 J. W. Fu, K. X. Jiang, X. Q. Qiu, J. G. Yu and M. Liu, *Mater. Today*, 2020, **32**, 222–243.
47 Z. Li and Y. G. Sun, *J. Mater. Chem. A*, 2013, **1**, 6786–6793.
48 B. Cai, J. Wang, D. X. Han, S. Y. Gan, Q. X. Zhang, Z. J. Wu and L. Niu, *Nanoscale*, 2013, **5**, 10989–10995.
49 J. H. Yang, Y. Z. Guo, W. Z. Lu, R. B. Jiang and J. F. Wang, *Adv. Mater.*, 2018, **30**, 1802227.
50 Y. A. Wu, I. McNulty, C. Liu, K. C. Lau, Q. Liu, A. P. Paulikas, C.-J. Sun, Z. H. Cai, J. R. Guest, Y. Ren, V. Stamenkovic, L. A. Curtiss, Y. Z. Liu and T. Rajh, *Nat. Energy*, 2019, **4**, 957–968.
51 Y.-C. Hao, L.-W. Chen, J. N. Li, Y. Guo, X. Su, M. Shu, Q. H. Zhang, W.-Y. Gao, S. W. Li, Z.-L. Yu, L. Gu, X. Feng, A.-X. Yin, R. Si, Y.-W. Zhang, B. Wang and C.-H. Yan, *Nat. Commun.*, 2021, **12**, 2682.
52 Y. N. Bo, C. Gao and Y. J. Xiong, *Nanoscale*, 2020, **12**, 12196–12209.
53 L. J. Liu, Y. Q. Jiang, H. L. Zhao, J. T. Chen, J. L. Cheng, K. S. Yang and Y. Li, *ACS Catal.*, 2016, **6**, 1097–1108.
54 J. Li, W. F. Pan, Q. Y. Liu, Z. Q. Chen, Z. J. Chen, X. Z. Feng and H. Chen, *J. Am. Chem. Soc.*, 2021, **143**, 6551–6559.
55 S. N. Habisreutinger, L. Schmidt-Mende and J. K. Stolarczyk, *Angew. Chem., Int. Ed.*, 2013, **52**, 7372–7408.
56 L. M. Wang, W. L. Chen, D. D. Zhang, Y. P. Du, R. Amal, S. Z. Qiao, J. B. Wu and Z. Y. Yin, *Chem. Soc. Rev.*, 2019, **48**, 5310–5349.
57 G. Kresse and J. Furthmüller, *Phys. Rev. B: Condens. Matter Mater. Phys.*, 1996, **54**, 11169–11186.
58 G. Kresse and J. Furthmüller, *Comput. Mater. Sci.*, 1996, **6**, 15–50.
59 G. Kress and D. Joubert, *Phys. Rev. B: Condens. Matter Mater. Phys.*, 1999, **59**, 1758–1775.
60 P. E. Blöchl, *Phys. Rev. B: Condens. Matter Mater. Phys.*, 1994, **50**, 17953–17979.
61 J. P. Perdew, K. Burke and M. Ernzerhof, *Phys. Rev. Lett.*, 1996, **77**, 3865–3868.

